Defect-like Packing and Structural Disorder in Monoatomic Metallic Glasses

Adil Houba[1,*], Mohamed El Ayoubi[1], Achraf Atila[2], Abdellatif Hasnaoui[1,**]

[1] *LS2ME Laboratory, Polydisciplinary Faculty of Khouribga, Sultan Moulay Slimane University of Beni Mellal, B.P. 145, Khouribga 25000, Morocco*
[2] *Federal Institute of Materials Research and Testing (BAM), Unter den Eichen 87, Berlin 12205, Germany*

Abstract

The quasi-nearest atom (QNA) parameter has shown promise in characterizing packing disorder in metallic glasses, yet its application has so far been limited to multicomponent alloys, where compositional complexity obscures the purely geometric nature of the defects it identifies. Here, we use QNA to identify structural defects in monoatomic metallic glasses produced by molecular dynamics simulations and assess their impact on mechanical behavior. We show that loosely packed atoms share similar structural signatures, including disrupted medium-range order, unusual ~90° bond angles, reduced five-fold symmetry, and a preference for energetically unfavorable 2- and 4-atom connection modes. When subjected to uniaxial tension, glasses with a lower density of loosely packed atoms exhibit superior mechanical properties. Regions with few QNA per atom constitute load-bearing backbones supporting high von Mises stress with limited shear strain, while high-QNA regions accommodate greater plastic deformation at lower stress and serve as preferential sites for shear transformation zones. The normalized QNA distributions collapse onto a single curve across the four FCC and BCC monoatomic glasses studied, with consistent spatial correlations and connection-mode fractions (within ±4%) at each N_Q level, suggesting that the packing topology is dominated primarily by geometry rather than by element-specific bonding. These results confirm that QNA is a promising structural descriptor for capturing important trends linking local packing geometry to mechanical behavior in monoatomic MGs.

Keywords: *Molecular dynamics, Monoatomic metallic glasses, quasi-nearest atom, Connection modes, Honeycutt–Andersen.*

*) Corresponding author: adil.houba@usms.ac.ma

**) Corresponding author: hasnaoui59@hotmail.com

1. Introduction

Metallic glasses (MGs), first discovered in the 1960s [1], are a type of disordered material typically prepared by rapid quenching of supercooled liquids, and inevitably inherit intrinsic structural heterogeneities as well as a large number of extrinsic casting defects [2–5]. They have garnered significant attention due to their exceptional mechanical properties, including ultrahigh strength, superior elasticity, and thermo-plasticity [6–9]. However, their industrial applications remain constrained by challenges such as limited ductility at room temperature and difficulties in fabricating macroscopic samples without crystallization [10, 11]. While significant ductility and strength have been reported for microscopic samples [12, 13], understanding the atomic-scale origins of defects and disorder in these amorphous systems remains a critical hurdle [14, 15].

Monoatomic MGs, although representing the simplest form of MG, have long posed a formidable challenge due to the intrinsic tendency of pure metals to crystallize rapidly. Early theoretical work by Turnbull [16] predicted that any liquid, including pure metals, should be able to form a glass if cooled fast enough to bypass nucleation and crystal growth. However, the experimental realization of MGs initially focused on multicomponent alloys, in which added chemical complexity and atomic size mismatch frustrate crystallization, thereby enhancing the glass-forming ability (GFA) [17]. Monoatomic MGs require extremely high cooling rates ($>10^{13}$ K/s), often several orders of magnitude higher than those required for alloys to suppress nucleation of the crystal phase, since they do not fulfill the conditions in the multicomponent alloys, such as the confusion principle [18], mixing enthalpy, and atomic size mismatch [19]. This challenge was recently addressed by Zhong et al. [20], who achieved the vitrification of several pure body-centered cubic (BCC) metals (Ta, V, W, and Mo) by employing cooling rates on the order of 10^{14} K/s in a transmission electron microscope. Building on these results, Tong et al. [21] later demonstrated a novel approach using picosecond pulsed laser ablation in a liquid medium (ethanol) to vitrify monoatomic metals with face-centered cubic (FCC) and hexagonal close-packed (HCP) structures. The ethanol medium not only facilitates rapid cooling but also minimizes heterogeneous nucleation by eliminating the typical liquid-crystal interface. These breakthroughs have not only provided experimental confirmation that monoatomic metals can form glass but have also opened new opportunities to explore the fundamental mechanisms of glass formation and identify the atomic-scale defects in these materials, free from the complicating factors present in multicomponent systems [7, 22–24].

Several structural indicators for MGs have been proposed and employed; the most common are the free volume [25], atomic-level stresses [26], fictive temperature [27], configurational potential energy [28], and topological local order (such as icosahedral order) [7, 15, 29, 30]. Although each of these measures offers valuable insights into the degree of disorder and stability of a metallic glassy state, they also have inherent limitations. Configurational potential energy and fictive temperature both represent the degree of disorder in a metallic glass (MG) state and serve as useful thermodynamic indicators of stability. However, these indicators provide only global system-averaged values that characterize the overall energetic or structural state of the MG without revealing the spatial distribution of disorder or identifying which specific atoms, clusters, or local atomic arrangements are responsible for that disorder [27, 28, 31]. Moreover, while these indicators can effectively compare the stability of MGs within the same composition, their utility across different compositions is unreliable because reference states for different alloys and materials are arbitrary. The free volume concept is a widely used structural parameter, defined on a per-atom basis as the excess volume relative to a reference state with zero free volume. While this concept works well for hard-sphere models and polymeric glasses, it is less suitable for materials with softer interatomic potentials, such as MGs, where the reference state is ambiguous and difficult to access [26]. Consequently, free volume is difficult to identify and quantify in these systems [32–34] since an atom in these systems does not have an indefinite volume. Moreover, although regions of high free volume may coincide with structural defects, the total free volume does not directly correspond to the number of defects [35]. For instance, during compressive deformation, the overall free volume can decrease even as the number of structural defects increases, underscoring that free volume alone is insufficient to fully describe the atomic-scale structural changes in MGs.

To overcome these challenges, Pan et al. [36, 37] proposed the quasi-nearest atom (QNA) parameter, a geometry-based metric that describes local packing and reveals structural defects in metallic liquids and glasses. The QNA parameter is particularly effective for detecting loosely packed clusters. To date, however, its application has been mainly confined to multicomponent alloys, where compositional complexity and atomic size mismatch can confound the interpretation of QNA-identified packing defects [38–41]. In the present study, we extend the application of QNA beyond multicomponent alloys to four monoatomic MGs of FCC Cu and Ni and BCC Fe and Ta, using large-scale molecular dynamics simulations. We quantify and compare packing disorder across these systems and then correlate the QNA parameter with both short- and medium-range structural signatures, employing Voronoi

tessellation, bond-angle analysis, Honeycutt–Andersen analysis, and spatial-correlation metrics. Finally, we perform uniaxial tensile simulations to establish a direct link between QNA identified structural defects and mechanical response, demonstrating how local packing geometry governs plastic deformation behavior in these monoatomic MGs.

2. Methodology

Molecular dynamics (MD) simulations were performed with the Large-scale Atomic/Molecular Massively Parallel Simulator (*LAMMPS*) [42] to prepare and analyze monoatomic MGs. The interatomic interaction was described using the realistic embedded-atom method (EAM) potential. The selected metals and their respective interatomic potentials include: FCC metals, Cu and Ni, modeled using those of Mendelev et al. [43] and Mishin [44], with systems containing 256,000 atoms, and BCC metals, Fe and Ta, modeled using those of Mendelev et al. [45] and Ravelo et al. [46], with systems containing 250,000 atoms. The samples were heated from 300 K to 1660 K (Cu), 2600 K (Ni), 2500 K (Fe), and 4000 K (Ta), temperatures exceeding their melting points, equilibrated for 1000 ps, and subsequently quenched to 300 K at a cooling rate of 10^{13} K/s, while maintaining a pressure of around 0 bar. The glassy samples at 300 K were then relaxed for 1500 ps in the NPT ensemble prior to loading, producing what we refer to as the "as-quenched glasses". *Fig. 1(a-b)* illustrates this transformation for Ni, from the initial FCC crystal (*Fig. 1(a)*) to the resulting as-quenched glass (*Fig. 1(b)*). Then, uniaxial tensile tests were carried out at 300 K at a constant strain rate of 10^{8} s^{-1} by deforming the sample along the y-direction, while maintaining zero pressure along the x- and z-directions [47–49]. A time step of 0.001 ps was used for the MD simulations, and periodic boundary conditions (PBC) were applied in all three dimensions for each sample. The Nosé-Hoover thermostat and barostat were used to control temperature and pressure.

The analysis of the structure of the obtained glasses was performed using Voronoi analysis, as implemented in the Open Visualization Tool (OVITO) [50], using both its graphical user interface and its Python programming interface, to calculate the number of QNAs for each atom [36, 37, 51]. A pair of atoms is defined as QNAs if the following three conditions are satisfied: (1) they share a common nearest neighbor; (2) their corresponding Voronoi cells centered on the common neighbor share an edge, and (3) they are not themselves nearest neighbors. When constructing the Voronoi polyhedra, issues related to degeneracy and thermal vibrations can arise, so we allow some flexibility under these conditions. These criteria are illustrated in *Fig. 1(c-f)* for clarity. In *Fig. 1(c)*, although the two cells share a small face, we consider them a pair of QNAs because surfaces with very small areas have been deliberately excluded. This

exclusion ensures that the pair of particles is not considered close neighbors, in turn respecting all the criteria for QNAs. In *Fig. 1(d)*, the two Voronoi cells do not exactly share an edge, but since the distance between the two edges is very small, we consider them as a pair of QNAs. In contrast, in *Fig. 1(f)*, the large distance disqualifies the atoms from being considered as a pair of QNAs. Additionally, in *Fig. 1(e)*, cells sharing only a vertex or a very small edge will not be considered as a pair of QNAs in this work. As Niu et al. [51] demonstrated, there is a large free volume between QNA pairs. Therefore, QNAs can be used to describe structural defects in monoatomic MGs.

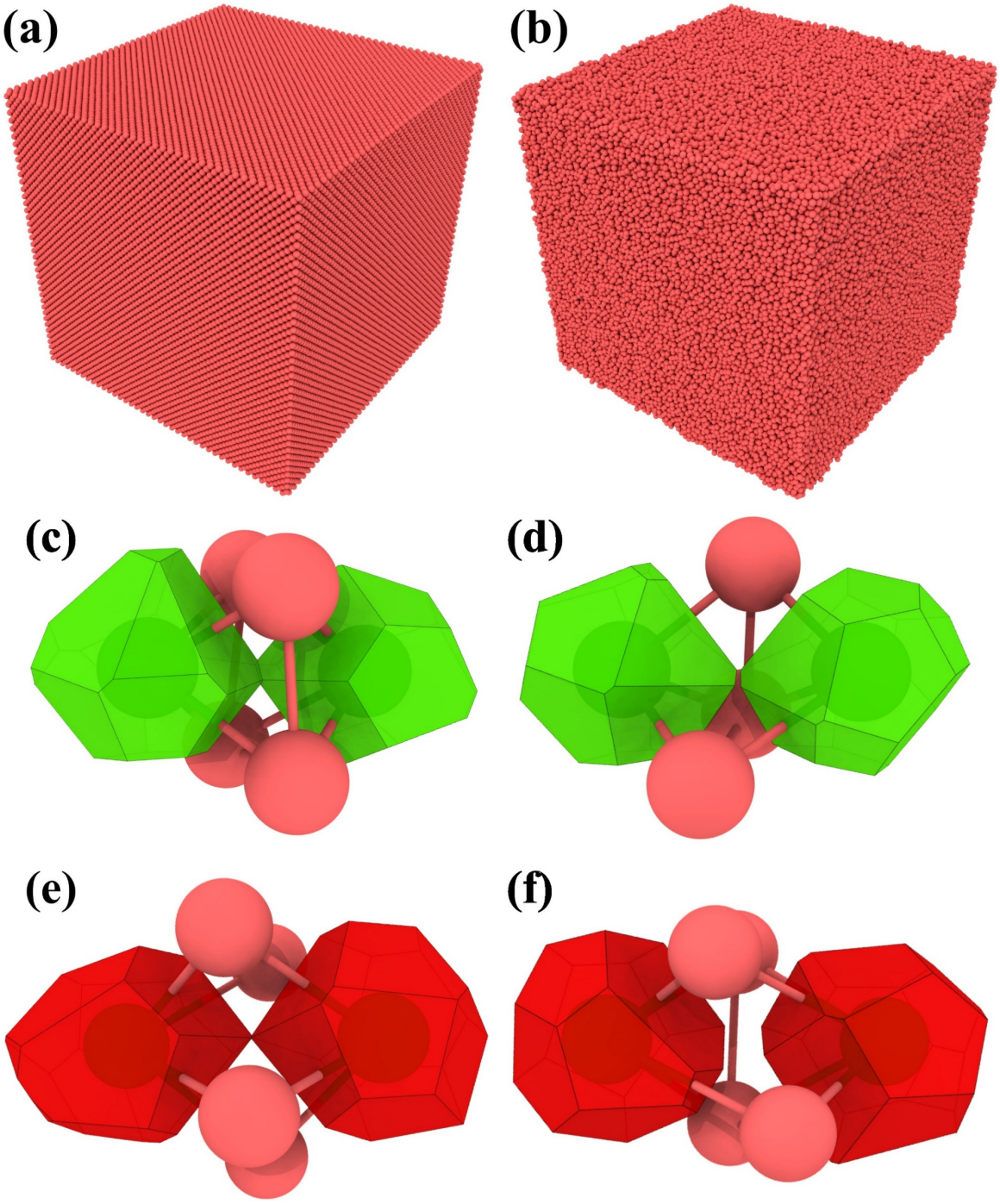

Fig. 1: Representative atomic snapshots of Ni in (a) the initial FCC crystalline state and (b) the as-quenched amorphous state. (c–f) Schematic description of QNA atoms, where the green cells (c, d) represent pairs of QNA and the red cells (e, f) correspond to non-QNA pairs.

3. Results

3-1. Distribution of the number of QNAs

QNA is an effective parameter for directly describing and quantifying local packing in metallic liquids and glasses [37, 51] and is closely linked to atomic packing density. A larger number of QNAs (N_Q) corresponds to looser atomic packing [37]. In *Fig. 2(a),* the distribution of N_Q in four model systems is presented. The distribution peaks at $N_Q = 1$ for Cu, Ni, and Fe MGs, with approximately 21.3%, 23.3%, and 32.9% of atoms, respectively, having no QNA. The distributions of QNA in Cu and Ni are nearly identical, indicating similar atomic packing densities. In comparison, the distributions for Ta and Fe MGs show a shift toward lower N_Q values. In particular, for Ta, the peak is at $N_Q = 0$, with approximately 48% of atoms having no QNA and less than 15% having $N_Q > 1$, making it more densely packed than the other three systems.

Fig. 2(b) presents the N_Q distributions of the Cu, Fe, Ni, and Ta MGs after subtracting the mean $\langle N_Q \rangle$ of each distribution and dividing by its standard deviation σ. This normalization collapses the four curves onto a single master curve, meaning that differences in mean and variance are absorbed, revealing a common underlying shape. In other words, atomic size, bond strength, and electronic structure do not alter the shape of the packing topology, which is governed by a statistical geometry common to the four monoatomic MGs. These findings are consistent with Pan et al. [37], who observed a universal scaled N_Q distribution in various metallic glass-forming liquids modeled using EAM at different temperatures.

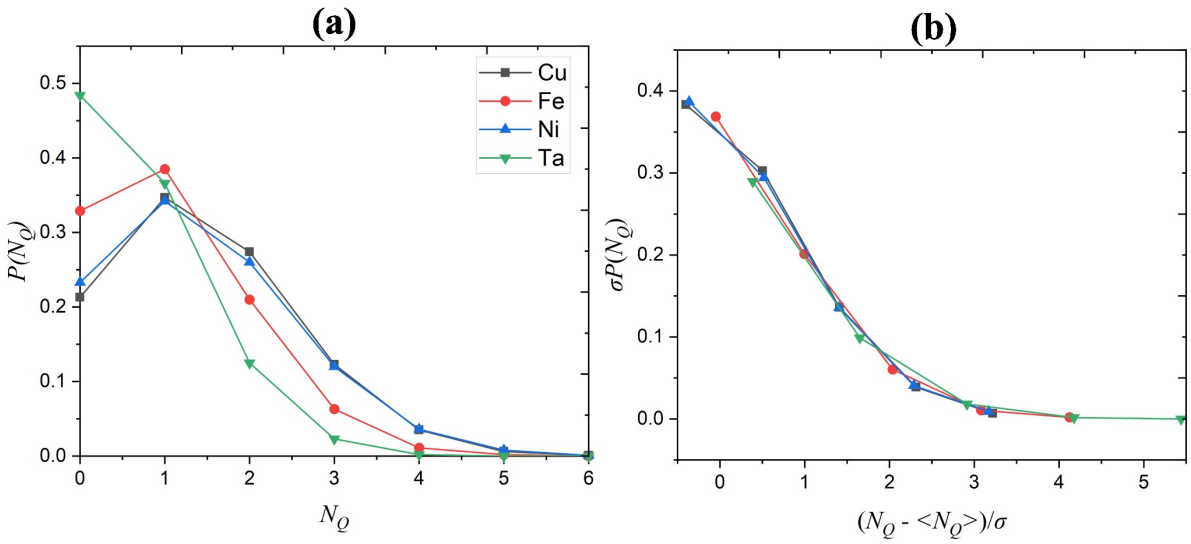

Fig. 2: (a) Distributions of N_Q, and (b) Normalized distributions of N_Q, shifted by the average value $\langle N_Q \rangle$ and scaled by the standard deviation σ, for Cu, Fe, Ni, Ta MGs

3-2. Radial Distribution Function

The partial radial distribution functions (RDFs) for different N_Q were computed in order to investigate their influence on the overall RDF of the system, focusing especially on the second RDF peak in Cu, Fe, Ni, and Ta MGs at 300 K. Analyzing subsets of atoms by N_Q shows how loosely and tightly packed atoms contribute to the overall structure.

Focusing on the total radial distribution function $g_{Total}(r)$, it was noted that the minimum height between the first and second peaks is 0.11, 0.12, 0.21, and 0.25 for Fe, Ta, Ni, and Cu MGs, respectively (*Fig. 3*). This means that the first and second peaks are more clearly separated in Fe and Ta MGs than in Ni and Cu MGs. Interestingly, the partial RDF of atoms with no QNA $g_{N_Q=0}(r)$ shows that this value reaches 0 in all monoatomic MGs, indicating that the two peaks are completely separated. However, an unusual peak appears near the first minimum in $g_{N_Q=2}(r)$ and becomes more pronounced in $g_{N_Q\geq3}(r)$. This suggests that atoms with high QNA are responsible for the ambiguity observed between the first and second peaks in the RDF of MGs. Additionally, in $g_{N_Q=2}(r)$ and $g_{N_Q\geq3}(r)$ the first peak is sharper, and the second peak is shifted to larger r values compared to the total RDF.

For loosely packed atoms, the first peak in RDF is sharp because their few remaining neighbors lie at nearly identical distances. In contrast, the total RDF shows that the nearest-neighbor distances are broadly distributed around the bond length characteristic of the corresponding

crystalline phase. As N_Q increases, the subset of atoms under consideration becomes progressively smaller (for example, $N_Q = 1$ includes more atoms than $N_Q = 2$, which includes more than $N_Q = 3$, etc.), so computing the RDF only over this shrinking subset further isolates those uniform neighbor distances. When all atoms are included, representing a wider variety of local environments, the RDF encompasses a wider range of neighbor distances, which broadens and lowers the height of the first peak. Thus, the subset-only RDF yields a high intensity first peak in $g_{N_Q \geq 3}(r)$ that directly reflects the uniform spacing among these loosely packed atoms. Furthermore, in $g_{N_Q \geq 3}(r)$ the emergence of an intermediate peak between the first and second peaks reflects a disruption of medium-range order (MRO), consistent with the less constrained and more irregular arrangement of atoms in these regions.

Previous studies have shown that the left sub-peak of the second peak in RDF corresponds to the 3-atom connection mode, while the right sub-peak corresponds to the 1-atom connection mode [52–54]. The 2-atom connection mode is hidden between the two sub-peaks, and the 4-atom connection mode is hidden between the first minimum and the left sub-peak due to their lower fractions in the system [52–54]. Focusing on the second peak, in $g_{N_Q=0}(r)$ a more pronounced split was observed (arrow in *Fig. 3(a)*). This hints that these atoms tend to adopt the 3-atom connection mode, with reduced contributions from the 2-atom and 4-atom connection modes. For the $g_{N_Q=1}(r)$ curve, the second peak matches that of $g_{Total}(r)$ in Fe MG, while closely resembling it in Ta MG. However, for Ni and Cu MGs, $g_{N_Q=1}(r)$ shows a lower minimum and a higher intensity of the left sub-peak compared to $g_{Total}(r)$. For $g_{N_Q=2}(r)$ and $g_{N_Q \geq 3}(r)$, in addition to the appearance of the peak near the first minimum, the intensity of the left sub-peak decreases, and the second peak split becomes less evident in all systems. These results suggest that atoms with high N_Q value do not favor the 3-atom connection mode but instead prefer the 2-atom and 4-atom connection modes.

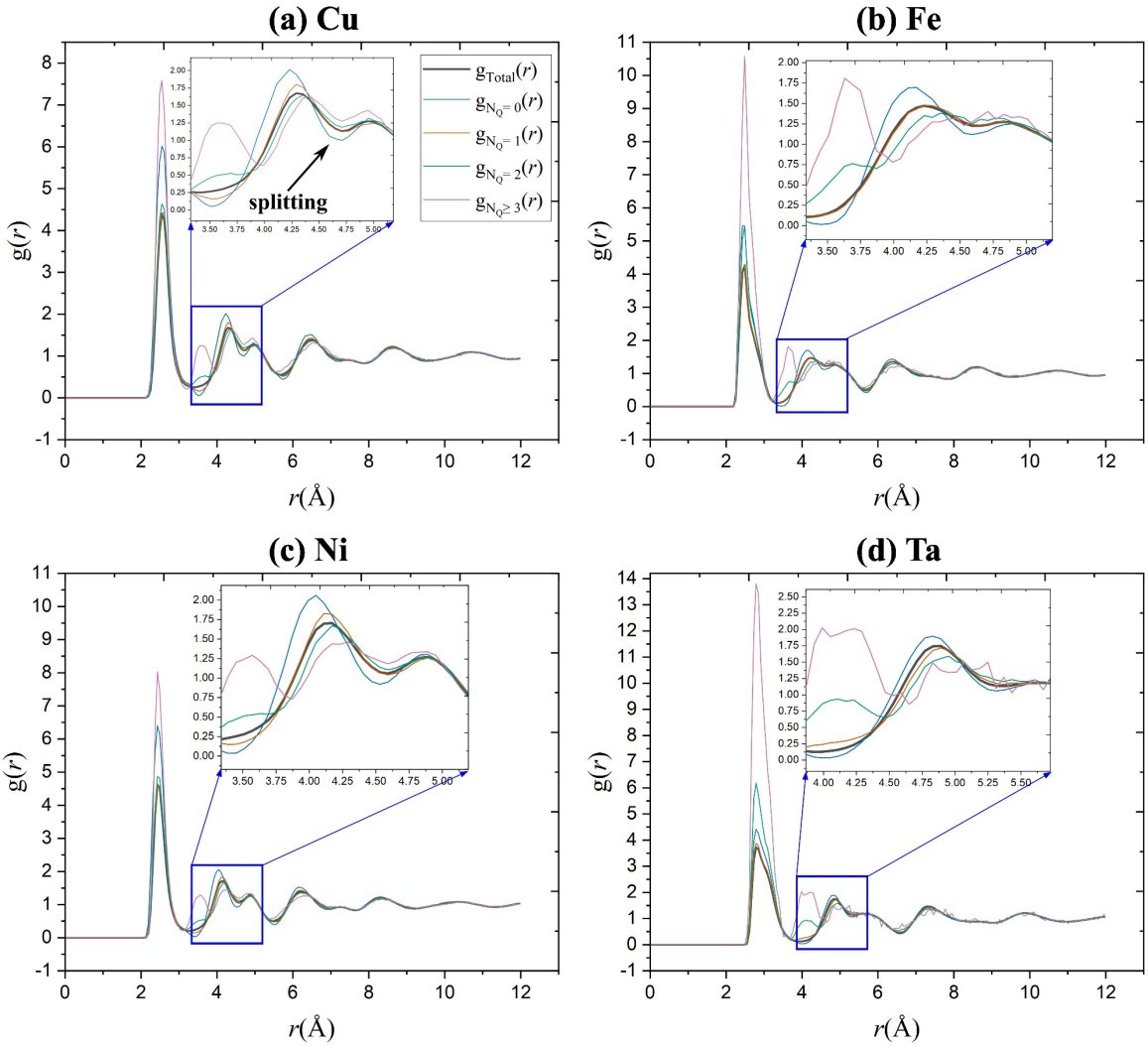

Fig. 3: Total and partial distribution functions ($g_{N_Q=0}(r)$, $g_{N_Q=1}(r)$, $g_{N_Q=2}(r)$ *and* $g_{N_Q\geq 3}(r)$) *for (a) Cu, (b) Fe, (c) Ni and (d) Ta MGs.*

3-3. Bond angle distributions

The interactions between neighboring atoms are more accurately described using bond angle distribution (BAD), which represents the distribution of bond angles formed by pairs of bonds converging at the same atom within the first coordination shell. This analysis considers only bonded particles; non-bonded pairs are ignored. To further investigate these interactions, the atoms were classified according to their N_Q value so that atoms with a low N_Q value (N_Q = 0) are referred to as N_{LQ}, while those with a high N_Q value (N_Q > 1) are referred to as N_{HQ}. The total number of angles in each triplet was used to normalize its BAD. For N_{LQ}-centered atoms, the BAD shows three main peaks at θ ≈ 60˚,110˚, 150˚, and a broad shoulder at 170˚-180˚ (*Fig. 4(d–f)*). Three of these peaks align with the peak locations associated with icosahedral short-

range order (SRO), namely $\theta = 63.5^{\circ}$, $\theta = 116.5^{\circ}$, and $\theta = 180^{\circ}$ [55, 56]. The remaining peak near $\theta = 150^{\circ}$ is not attributed to icosahedral SRO but reflects the structural adjustment of the surrounding atoms to the icosahedral network. Conversely, for N_{HQ}-centered atoms, the flat peak at high angles disappears (*Fig. 4(a–c)*), implying weaker icosahedral order around these atoms. For N_{HQ}-N_{HQ}-N_{HQ} triplets specifically, the calculated BADs show a new peak around $\theta = 90^{\circ}$ that merges with the usual peak at $\theta = 110^{\circ}$. This new peak appears stronger in BCC-type glassy metals Ta and Fe. From previous work [55], the bond angle distribution in FCC crystals includes $\theta = 60^{\circ}$, 90°, 120°, and 180°. Moreover, Ganesh et al. [57] reported that crystallographic clusters (FCC, HCP, or BCC) exhibit bond angles of ~60°, 90°, and 120°. Thus, the new peak at $\theta = 90^{\circ}$ could be attributed to crystal-like atoms within the amorphous structure, reflecting a partial alignment of bond angles characteristic of crystalline phases. Taken together with the residual icosahedral signatures, this indicates a mixture of icosahedral and FCC/BCC-like crystalline ordering, in which loosely packed regions do not fully adopt either structural motif. This is consistent with the previous RDF analysis, which showed that atoms with high N_Q values exhibit disrupted MRO likely driven by the geometric distortions revealed in the BADs of N_{HQ}–N_{HQ}–N_{HQ} triplets.

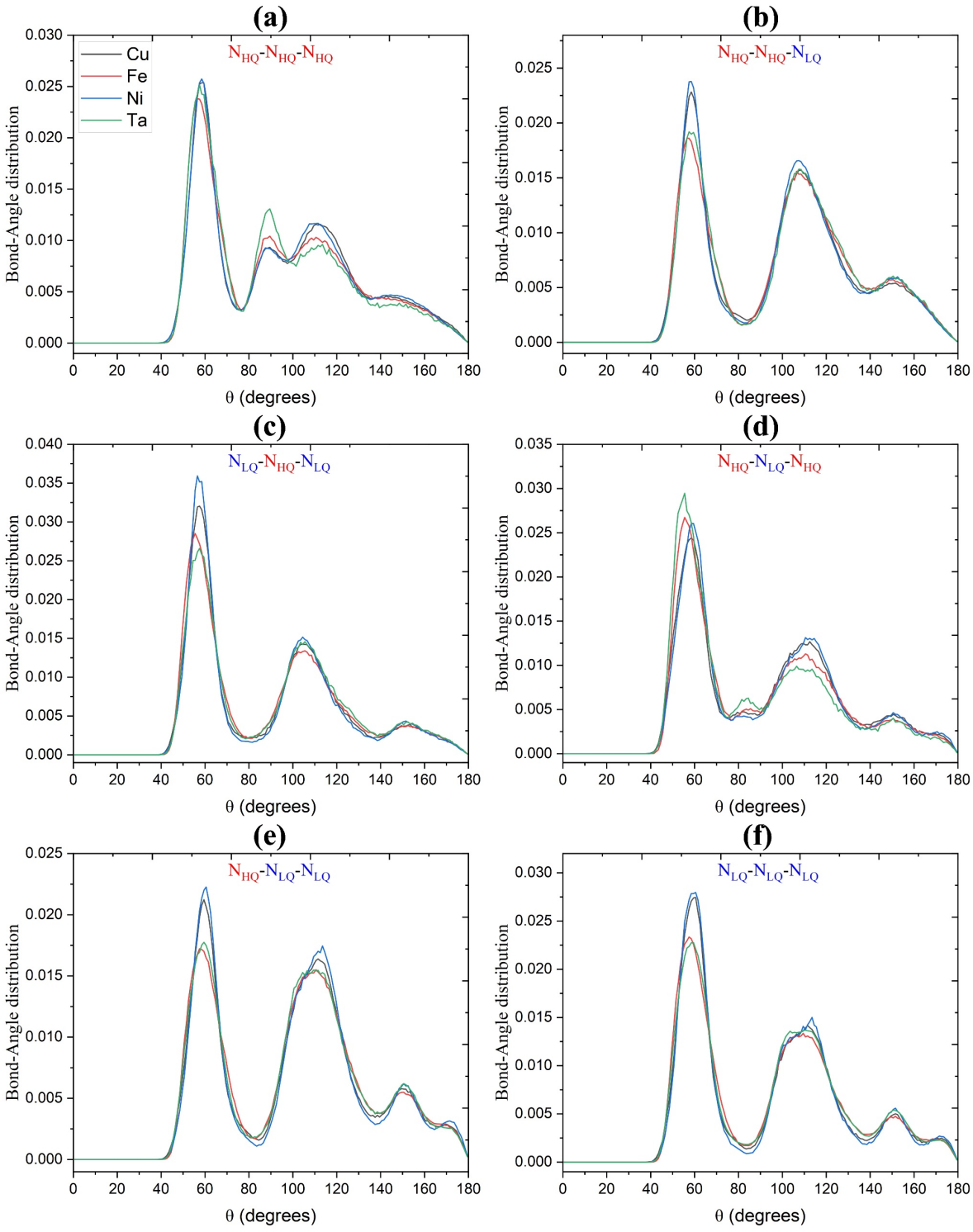

Fig. 4: (a-c) Partial *BADs* of the N_{HQ}-centered triplets (N_{HQ}–N_{HQ} –N_{HQ}, N_{HQ}–N_{HQ} –N_{LQ}, and N_{LQ}–N_{HQ} –N_{LQ}); *(d-f)* presents the partial *BADs* of N_{LQ}-centered triplets (N_{LQ}–N_{LQ}–N_{LQ}, N_{HQ}–N_{LQ}–N_{LQ}, and N_{HQ}–N_{LQ}–N_{HQ}) in *Cu*, *Fe*, *Ni*, and *Ta* MGs.

3-4. Spatial distribution of QNA

To examine the spatial distribution of QNA, we investigated the space correlation function (*scf(r)*) for N_Q, defined as follows [38, 51]:

$$scf(r) = \frac{1}{N}\sum_{i=1}^{N}\frac{(N_Q(i) - \langle N_Q\rangle)(\langle N_Q(i,r,r+dr)\rangle - \langle N_Q\rangle)}{D(N_Q)^2} \quad (1)$$

Here $N_Q(i)$ is the QNA count for atom i, while $\langle N_Q\rangle$ and $D(N_Q)$ are the system's average and standard deviation, respectively. The value of $scf(r)$ ranges between -1 and 1, where larger $|scf(r)|$ values indicate stronger spatial correlation, and values near 0 imply negligible correlation.

The spatial correlation function (*scf(r)*) for N_Q in these monoatomic MGs is shown in *Fig. 5(a)*. For Ni, Cu, and Fe MGs, spatial correlation begins at around 2 Å, while for Ta MG it starts around 2.3 Å, reflecting Ta's larger interatomic spacing. After onset, *scf(r)* increases rapidly, then decreases to near zero, followed by another rise to a maximum value before declining again and stabilizing close to zero, indicating minimal spatial correlation for N_Q beyond this point. Consequently, the spatial correlation length (SCL) for N_Q is approximately 4.5 Å, 4.0 Å, 4.1 Å, and 4.9 Å for Cu, Fe, Ni, and Ta MGs, respectively. The *scf(r)* patterns for all four MGs suggest that N_Q behaves in a qualitatively similar way across different systems, consistent with a common underlying packing geometry as previously noted by Pan et al. [37].

To highlight spatial heterogeneity in QNA, we adopted a voxel-grid coarse-graining approach. Each voxel was assigned a coarse-grained AN_Q value obtained by averaging the N_Q of an atom and its neighbors within the SCL. The voxelized AN_Q values were color-coded in *Fig. 5(b-e)* for Cu, Fe, Ni, and Ta MGs. The resulting configurations reveal clear spatial heterogeneity, with atoms having higher or lower AN_Q values preferring to cluster together. To quantify this clustering, we computed the global Moran's I index [58, 59], a well-known spatial autocorrelation metric that measures the extent to which similar AN_Q values are spatially clustered. In three dimensions (*3D*), Moran's I is defined as:

$$I_{3D} = \frac{N}{S_0}\frac{\sum_{i=1}^{N}\sum_{j=1}^{N}\partial_{ij}(AN_Q(i) - \langle AN_Q\rangle)(AN_Q(j) - \langle AN_Q\rangle)}{\sum_{i=1}^{N}(AN_Q(i) - \langle AN_Q\rangle)^2} \quad (2)$$

Where N is the total number of voxels (with $N = d_1 \times d_2 \times d_3$), and the total number of contiguous face-sharing pairs is $S_0 = 6N/2 = 3N$, since each voxel has 6 neighbors, counted once per pair, the binary weight ∂_{ij} is equal to 1 if voxels i and j share a face (applying periodic boundaries), otherwise 0, and $\langle AN_Q \rangle$ is the system's average of AN_Q. In a grid with dimensions larger than 30×30×30, the expected value of Moran's I_{3D} under spatial randomness should be zero, meaning no spatial autocorrelation. Hence, a computed I_{3D} greater than zero indicates significant clustering of similar AN_Q values, whereas a negative value indicates dispersion.

The statistical analysis in *Table 1* shows distinct differences in the AN_Q distributions across the four monoatomic MGs. Statistical descriptors (mean, variance, standard deviation, skewness) were calculated from the distribution of AN_Q values across all voxels. Moran's I_{3D}, on the other hand, accounts for spatial adjacency relationships in the 3D voxel grid. We also used two skewness metrics to quantify the asymmetry of the AN_Q distributions. The Fisher-Pearson skewness (g_1) is defined as:

$$g_1 = \frac{1}{N\sigma^3} \sum_{i=1}^{N} \left(AN_Q(i) - \langle AN_Q \rangle \right)^3 \tag{3}$$

This metric quantifies asymmetry by weighting deviations from the mean with a cubic factor, making it sensitive to the behavior of the distribution tail. The Pearson Median Skewness (g_2) is defined as:

$$g_2 = \frac{3\left(\langle AN_Q \rangle - M_d \right)}{\sigma} \tag{4}$$

This metric measures asymmetry based on the difference between the mean and the median, making it less sensitive to extreme tail values. Here, $AN_Q(i)$ represents the coarse-grained N_Q value for voxel i, $\langle AN_Q \rangle$ is the mean, M_d is the median, σ is the standard deviation, and N is the total number of voxels.

Ta MG has the lowest variance (0.183) and standard deviation (0.428), which means most atoms are close to the low mean of 0.694. Notably, it exhibits the highest Fisher-Pearson skewness (0.691), followed by Fe-MG (0.584), Ni-MG (0.465), and Cu-MG (0.432). The positive Fisher-Pearson skewness values in all systems indicate asymmetric distributions with tails extending toward higher AN_Q values, suggesting the presence of atoms with high local free volume. Conversely, Ta MG exhibits the lowest Pearson Median Skewness (0.194). This

combination of high Fisher-Pearson skewness, low Pearson Median Skewness, and low variance implies that extreme free-volume defects form a long tail while the bulk distribution remains closely symmetric around the low free volume state. In other words, most atoms occupy low free volume environments, while a small fraction occupies more loosely packed regions. In contrast, Ni MG shows the highest variance (0.406) and standard deviation (0.637), indicating a greater dispersion of AN_Q values across the system. Regarding spatial clustering, Ta MG has the lowest Moran's I_{3D} (0.152) while Cu MG has the highest value (0.174), closely followed by Fe MG (0.171) and Ni MG (0.166). All Moran's I_{3D} values are positive, indicating that atoms with similar AN_Q values tend to cluster spatially. Previous studies have shown that Ta MG is rich in highly symmetric icosahedral-like clusters, with a five-fold symmetry that dominates its SRO [22, 60–63]. These icosahedral clusters interconnect into extended medium-range structures [30] that enhance local packing efficiency. Although intrinsic structural heterogeneities are inherent to all MGs [64], experimental studies by Zhang et al. [65] provided direct evidence for the intrinsic nature of structural heterogeneity in Ta monoatomic MG using amplitude-modulation dynamic atomic force microscopy, revealing its persistence despite annealing. However, they concluded that the degree of structural heterogeneity in monoatomic MGs is lower than that in multi-element MGs, which they attributed to the complexity of their chemical compositions. The role of free-volume heterogeneity in determining mechanical performance is complex and depends critically on both quantity and spatial distribution. While yield strength is primarily dependent on the overall amount of free volume, plasticity relies mainly on the distribution [66, 67]. Wide free-volume dispersion promotes the multiplication and branching of shear bands, thereby preventing catastrophic failure along a single dominant band [66, 68].

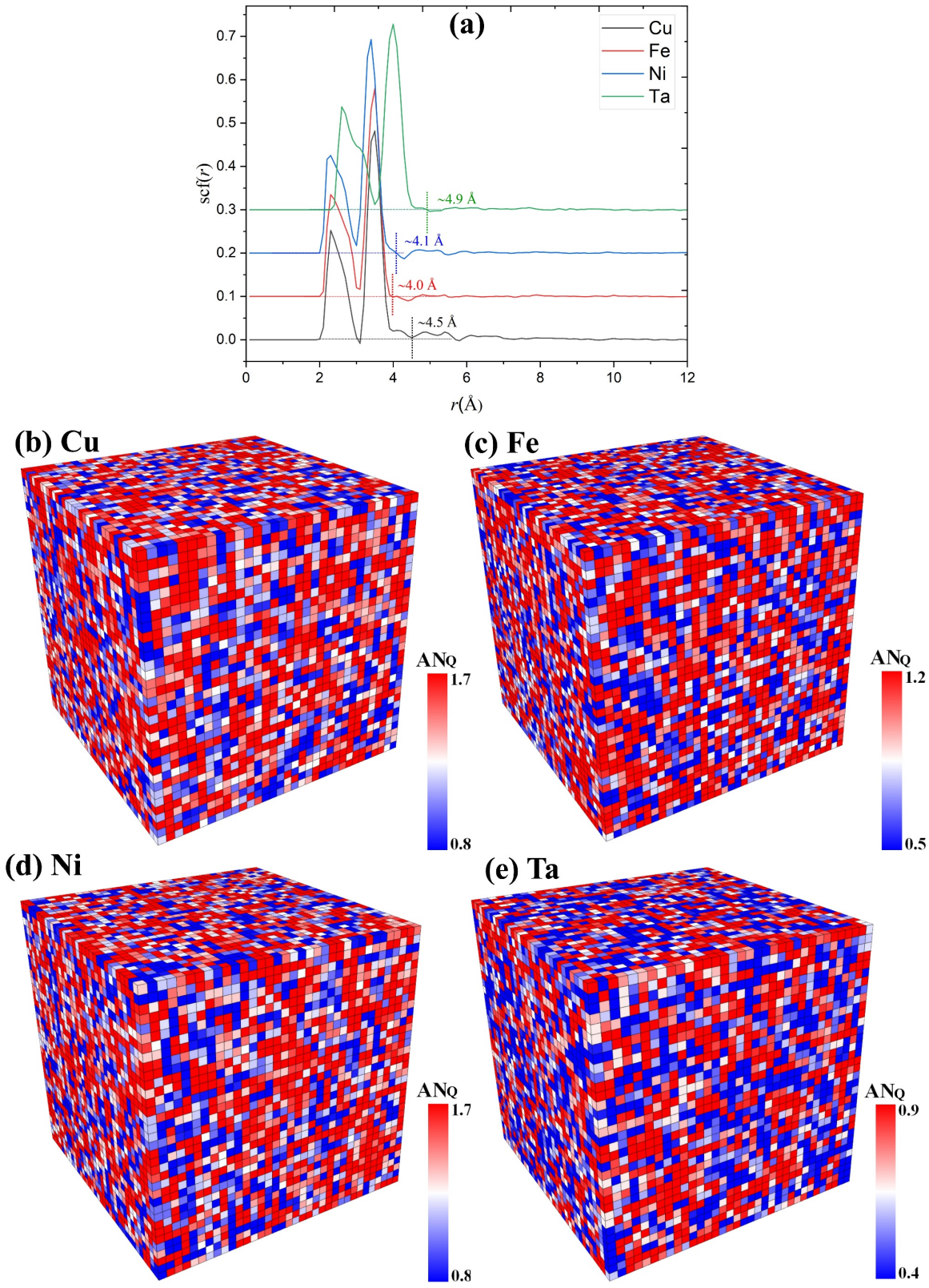

Fig. 5: (a) Spatial correlation function (scf(r)) and (b-e) Snapshots of configurations (b) Cu, (c) Fe, (d) Ni and (e) Ta MGs with atoms colored by different AN_Q

Table 1: Statistical descriptors of AN_Q distribution in monoatomic MGs.

	Cu	Fe	Ni	Ta
Fisher-Pearson Skewness	0.432	0.584	0.465	0.691
Pearson Median Skewness	0.222	0.275	0.386	0.194
mean	1.443	1.051	1.415	0.694
variance	0.344	0.313	0.406	0.183
standard deviation	0.586	0.559	0.637	0.428
Moran's I:	0.174	0.171	0.166	0.152

3-5. Voronoi Tessellation Analysis

We employed Voronoi Tessellation Analysis (VTA) to examine the local atomic structure of these amorphous materials. In this method, planes are drawn to bisect the lines connecting a center atom to each of its neighbors. The polyhedron enclosed by these planes is known as a Voronoi polyhedron (VP), and its geometry is characterized by four indices, n_i (i = 3, 4, 5, 6), which represent the number of i-edged faces of the VP. Additionally, by summing these indices (CN = $\sum n_i$) we can determine the coordination number (*CN*). Throughout this study, two atoms are considered neighbors if they share a common Voronoi face with an area above a minimum threshold (0.2 Å^2), thereby excluding small degenerate faces.

We then computed the mean number of quasi-nearest atoms ($\langle N_Q \rangle$) associated with each VP type. To compare polyhedra on a common scale, $\langle N_Q \rangle$ was normalized to the [0,1] range as shown in *Fig. 6*, using the following formula:

$$\langle N_Q \rangle_{normalized} = \frac{\langle N_Q \rangle - \langle N_Q \rangle_{min}}{\langle N_Q \rangle_{max} - \langle N_Q \rangle_{min}} \quad (5)$$

Based on their *CN*, we found that VPs can be classified into several groups. The perfect icosahedral polyhedron ⟨0,0,12,0⟩ consistently has the lowest $\langle N_Q \rangle$ among polyhedra, despite its relatively low *CN*, indicating an exceptionally high atomic packing density. Notably, these icosahedral clusters have the lowest formation energy and are much easier to form than other VPs [69], underscoring their critical role in stabilizing MGs, as their structure contributes significantly to overall packing efficiency and mechanical stability. The VPs with the highest CN = 15 (⟨0,2,8,5⟩ and ⟨0,1,10,4⟩) have the second lowest $\langle N_Q \rangle$, followed by VPs with CN = 14 (⟨0,1,10,3⟩, ⟨0,2,8,4⟩, ⟨0,3,6,5⟩) and the CN = 13 VP ⟨0,1,10,2⟩, displaying the third lowest $\langle N_Q \rangle$. Previous research by Guo [70] demonstrated that VP ⟨0,1,10,2⟩ retains many of the structural features of the ⟨0,0,12,0⟩ cluster, particularly in the connection modes of the shell

atoms, indicating a high degree of similarity to the ⟨0,0,12,0⟩ configuration, which in turn can explain its low ⟨N_Q⟩, even though it has a CN = 13.

Finally, VP ⟨0,3,6,4⟩ with CN = 13 shows the highest ⟨N_Q⟩ among the polyhedra considered. Besides *CN*, five-fold symmetry is another factor that affects atomic packing in MGs. For example, the ⟨0,3,6,5⟩ with the lowest five-fold symmetry among VPs with CN = 14, consistently shows the highest ⟨N_Q⟩. This suggests that when two atoms have the same *CN*, the atoms with higher five-fold symmetry are more likely to have a smaller N_Q. The higher degree of five-fold symmetry in these clusters enhances atomic immobility, thereby contributing to overall structural stability [71]. Li et al. [72] observed that irreversible atomic rearrangements during deformation tend to avoid regions with a high degree of five-fold symmetry and prefer to occur in areas with low five-fold symmetry.

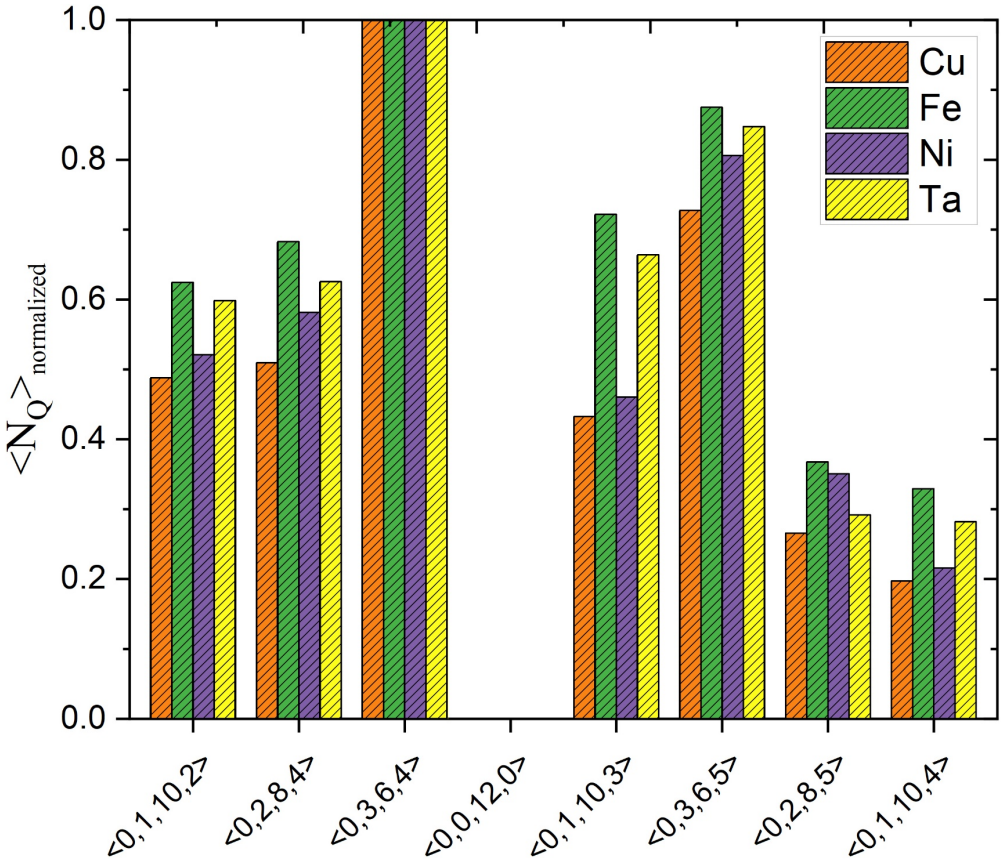

Fig. 6: $\langle N_Q \rangle_{normalized}$ *of top Voronoi polyhedrons in Cu, Fe, Ni,* and *Ta MGs at 300 K (⟨0,0,12,0⟩ = 0 by normalization).*

Fig. 7(d) shows a schematic visualization of a Voronoi polyhedron, where the green pentagonal faces (5 edges) directly contribute to the five-fold symmetry index n_5, blue faces represent quadrilaterals (4 edges), and red faces represent hexagons (6 edges). *Fig. 7(a-b)* shows how

average CN and five-fold symmetry index n_5 vary with N_Q across monoatomic MGs systems. A clear pattern emerges: as N_Q increases, CN and n_5 generally decrease, consistent with the study by Niu et al. [51]. However, in their study, they also observed an overlapping distribution of CN values, indicating that some atoms with higher CN may exhibit looser atomic packing (high N_Q), while others with lower CN may be more densely packed (low N_Q). We computed the center of mass for each polyhedron in our systems to determine the offset distance r_{offset} between the position of the central atom $r_{central}$ and the center of mass of its polyhedron r_{COM}, using the following equation:

$$r_{offset} = \|r_{central} - r_{COM}\| = \sqrt{\sum_{j=x,y,z} \left(r_{central,j} - r_{COM,j}\right)^2} \quad (6)$$

The average r_{offset} is then computed for atoms with N_Q = 0,1,2,3 and 4, as shown in *Fig. 7(c)*. The results reveal a clear trend in which r_{offset} increases as N_Q increases, suggesting that atoms with higher N_Q deviate more from the center of mass of their respective polyhedra, indicating increased structural asymmetry in their local environments. This observation is consistent with our earlier analyses, as high-N_Q atoms were associated with an unusual RDF peak and a ~90° bond-angle peak, confirming that they inhabit more distorted structures than low-N_Q atoms.

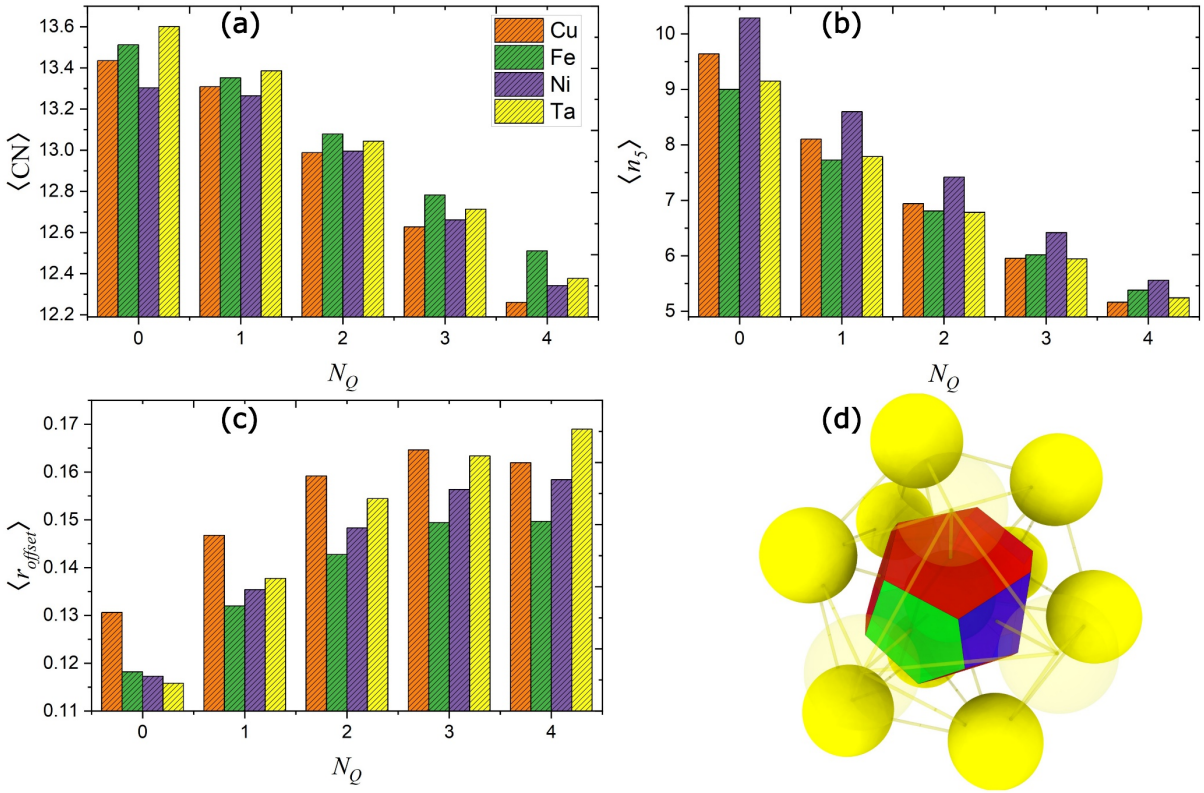

Fig. 7: *Average values of (a) CN, (b) n_5 and (c) r_{offset} plotted as functions of N_Q. (d) Schematic representation of a Voronoi polyhedron with coordinating atoms in yellow and polyhedral faces colored by edge number: blue for 4 edges, green for 5 edges, and red for 6 edges.*

To understand how second-shell atoms connect to central atoms through shared first-shell neighbors (*Fig. 8),* we calculated the fractional distribution of connection mode (1-, 2-, 3-, and 4-atom) for each N_Q group. Results are shown in *Fig. 9(a-d)*, which show that all four monoatomic systems exhibit similar trends. 3-atom connections (face-sharing) systematically decrease from 33-37% at $N_Q = 0$ to 21-23% at $N_Q = 4$, reflecting the loss of icosahedral packing, where atoms arranged in five-fold symmetric patterns naturally create many triangular connections; 2-atom connections (edge-sharing) correspondingly increase from 18-21% to 25-27%, indicating a shift toward less coordinated atoms, more disordered arrangements; and 4-atom connections increase from 2-5% to 8-9%, associated with frustrated arrangements in defective regions, distinct from the efficient triangular face-sharing characteristic of icosahedral order. In contrast, 1-atom connections show minimal variation (41.8-43.8%), because 1-atom connections (vertex-sharing) are present across diverse structural motifs and do not preferentially favor either dense packing or loose packing. It is worth noting that the connection-mode fractions vary by less than ±4% across Cu, Fe, Ni, and Ta MGs at each N_Q level, suggesting that these patterns depend on local packing geometry rather than on the specific element. From our previous study [53], 3-atom connections exhibit the lowest energy and dominate in stable MG structures, while 2- and 4-atom connections correlate with higher energy; thus, the drop in 3-atom fraction from $N_Q = 0$ (dense regions) to $N_Q = 4$ (highly defective regions) represents a progressive energetic destabilization of MRO. While Ta-MG's connection mode fractions closely match those of other MGs, its distinction lies in its higher count of second-nearest neighbors (CN_2) as shown in *Fig. 9(e)* (50.25 at $N_Q = 0$) combined with 48% of atoms occupying the $N_Q = 0$ state, where 3-atom connectivity dominates, creating a percolating network of stable, face-sharing connected regions that underlies its superior GFA. In other words, the atomic spacing in Ta MGs accommodates denser second-shell packing without the frustration that requires other MGs to distort slightly from $N_Q = 0$ to $N_Q = 1$ to maximize coordination, which allows Ta to optimize both local and extended structural order.

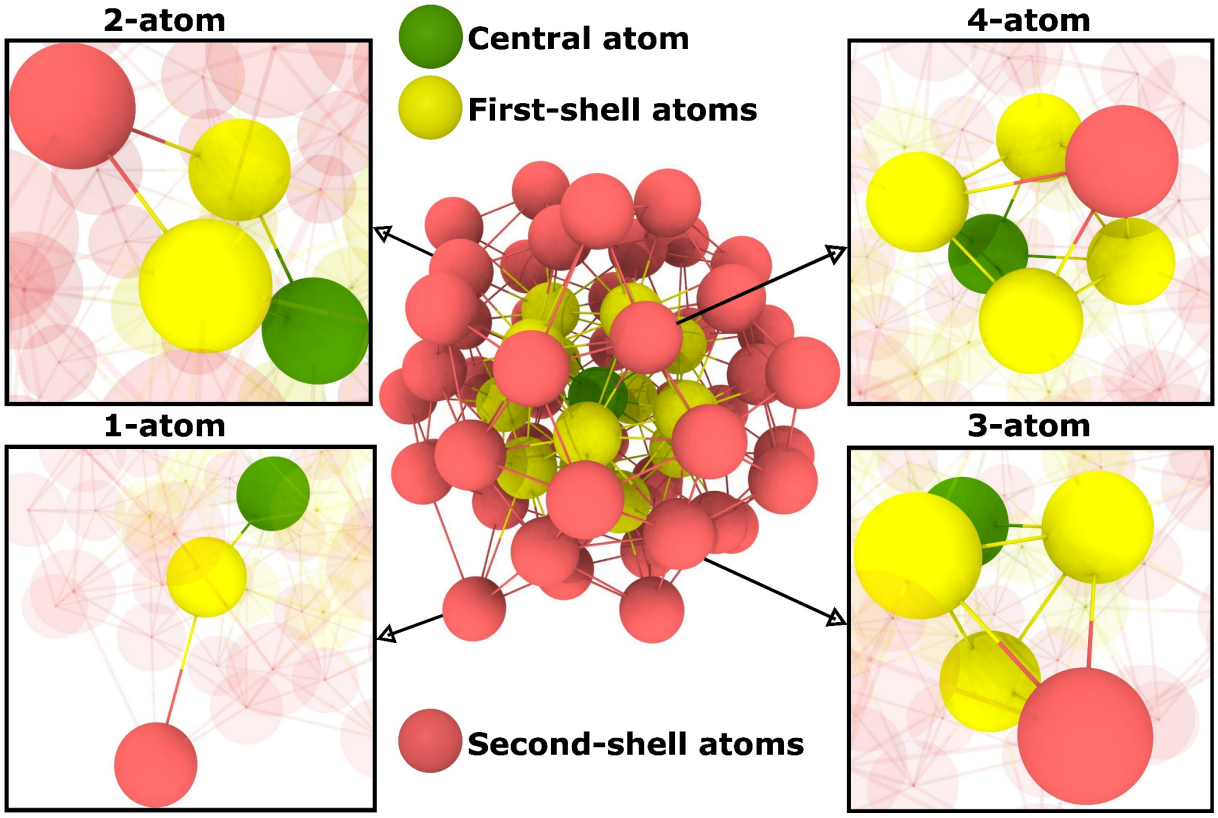

Fig. 8: *Visualization of 1-, 2-, 3-, and 4- atom connection modes between central atoms (green) and second-shell atoms (red) through shared first-shell neighbors (yellow).*

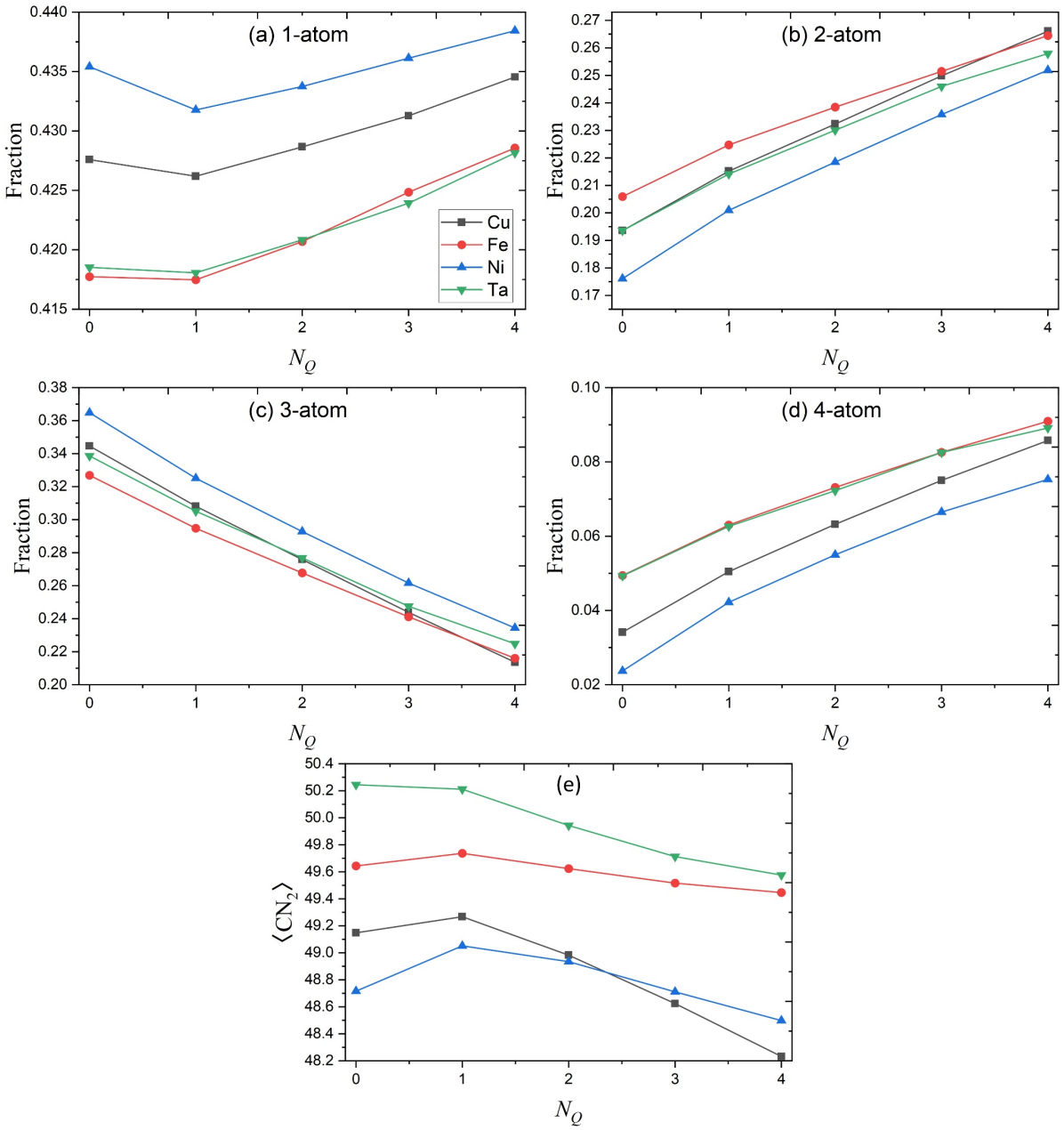

Fig. 9: *(a-d) Connection modes fractions and (e) average second-shell coordination as a function of N_Q for Cu, Fe, Ni, and Ta MGs.*

3-6. Honeycutt–Andersen pair analysis

To further examine the local microstructural arrangement, we applied the Honeycutt–Andersen (HA) pair analysis method [73]. This technique effectively identifies and distinguishes the different local structures present in the simulated systems. The HA index consists of four numbers (*i*, *j*, *k*, and *l*), each playing a specific role in characterizing the local structure. The first index indicates whether two atoms form a bonded pair, with a value of 1 signifying that the atoms are within each other's first coordination shell, while a value of 2 denotes a non-bonded pair. In our analysis, we focus on the non-bonded case. The second index is the count of nearest neighbors that the atom pair has in common, and the third index is the number of bonds among those shared neighbors. Because multiple local structures can share the same first three indices, a fourth index is used to distinguish among them. *Fig. 10(c)* shows some examples of HA indices.

Fractions of HA indices for local structures in different monoatomic MGs are shown in *Fig. 10(a)*. The findings indicate that although the fractions of different HA indices are generally similar across all MGs, there are small differences. The HA index 2101 has the highest fraction, followed by 2331 and 2211. The fraction of the 2451 pair is higher in BCC-type glassy metals, whereas 2441 and 2321 pairs are more prominent in *FCC*-type glassy metals. In contrast, the 2431 and 2311 pairs are nearly absent in all the monoatomic MGs studied. Since 2101 has the highest fraction, it implies that 1-atom connection mode is predominant, while the 4-atom connection mode is the least abundant, appearing as the 2441 and 2451 pairs. This observation is in good agreement with previously reported results [4, 53, 54]. The 2-atom connection mode, on the other hand, is primarily represented by the HA index for the 2211 pair, with the 2201 pair as another possible representation, though it does not appear in our systems. Meanwhile, the 3-atom connection mode primarily appears as the 2331 pair, with Ta showing the highest fraction of this pair. This 3-atom connection mode is also observed to a lesser extent as the 2321 and 2311 pairs. Ding et al. [52] studied the evolution of cluster connection patterns during cooling in $Cu_{64}Zr_{36}$ MGs and found that slower cooling rates favor an increase in the population of 1- and 3-atom connection modes while decreasing the population of 2- and 4-atom connection modes. This indicates that the relaxed amorphous structure obtained at a lower cooling rate with the lowest energy state contains more 1-atom and 3-atom connection modes. Previous MD simulations [52, 74] also indicate that the 1- and 3-atom connection modes exhibit greater resistance to deformation than the 2- and 4-atom connection modes.

Fig. 10(b) depicts the distribution of different QNA pair types. We observe that the 2441 pair is more frequent than the other QNA pairs, particularly in Ta and Fe MGs. The 2321 and 2431 pairs are the second- and third-most common QNA types, though their overall fraction in the system is very low, as shown in *Fig. 10(a).* Both pairs have index j greater than k, with *Ni* MGs showing higher numbers of these pairs. Two groups of bond pairs can be classified according to the correlation between j and k [41]. The bond pair is known as a "saturated bond pair" if j is less than or equal to k, meaning that the ring is formed by j common nearest neighbors or, in some cases, more (as observed with the 2451 pair). Conversely, if j is larger than k, it is termed an "unsaturated bond pair," implying the presence of gaps or holes in the ring. As a result, saturated bond pairs can be associated with a close atomic packing arrangement. To confirm this, *Table 2* presents the fractional distribution of QNA pairs across HA indices for Cu, Fe, Ni, and Ta. Among the 4-atom connection pairs, the unsaturated bond pair 2431 is almost entirely composed of QNA pairs, indicating that all 2431 pairs present are QNA pairs, while for the saturated bond pairs, approximately 72% of 2441 pairs and only about 2% of 2451 pairs are QNA across all systems. This result highlights that as the number of bonds between atoms increases, the packing of 4-atom connection pairs becomes denser. A similar trend is observed for the 3-atom connection pairs: the unsaturated bond pair 2321 has the lowest QNA fraction in Ta MGs at 32% and the highest in Ni MGs at 44%. Additionally, the 2311 pair is composed almost entirely of QNA pairs, whereas the saturated bond pair 2331 contains almost no QNA pairs (less than 0.2%) in all monoatomic MGs we analyzed. Furthermore, the absence of QNA pairs in the 2101 and 2211 pairs suggests that QNA is closely correlated with 4 and 3-atom connection modes.

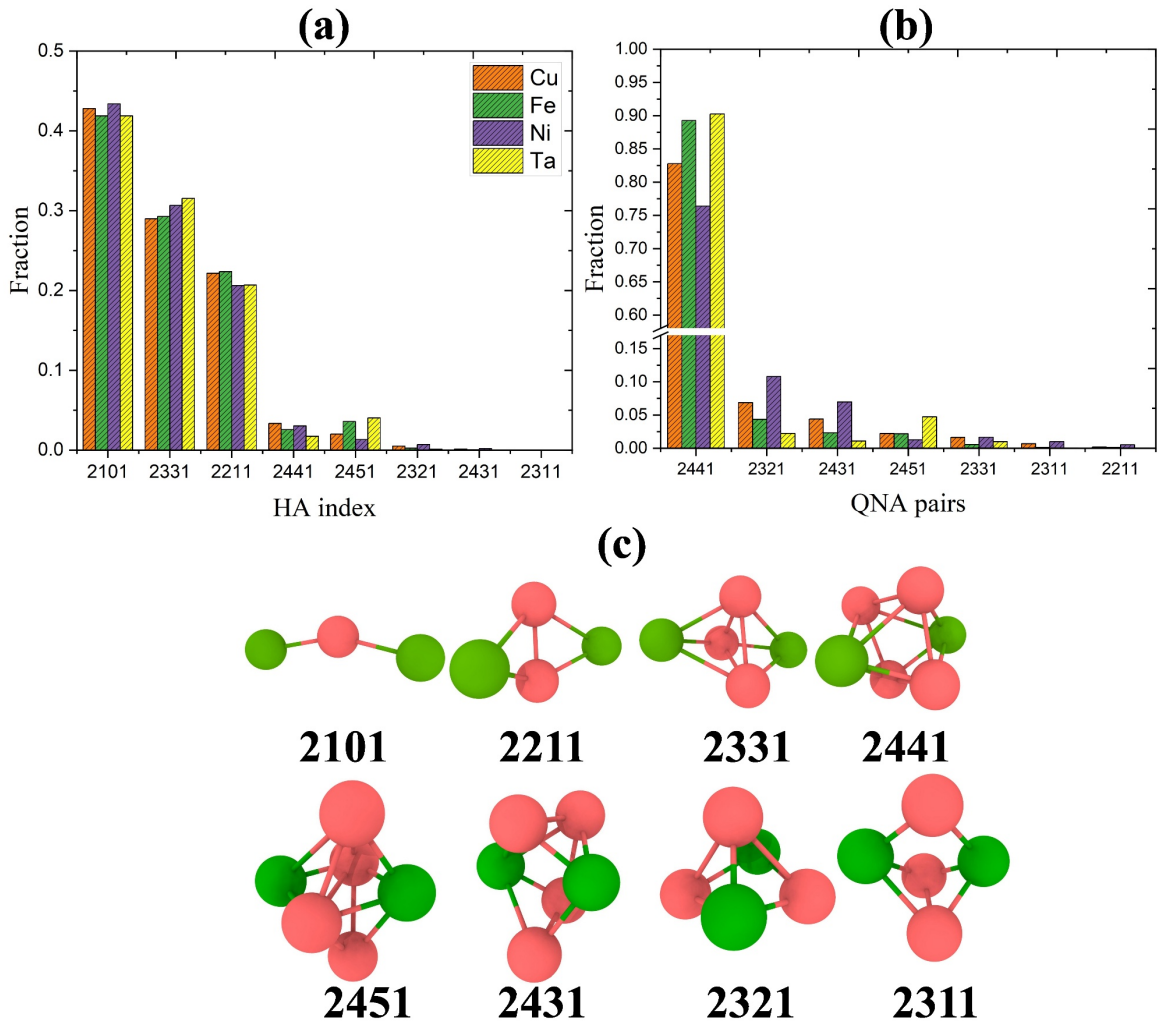

Fig. 10: (*a) HA index fractions and (b) Fraction of different QNA pairs types for Cu, Fe, Ni, and Ta MGs; (c) Schematic drawing of the related HA Indices with central atoms in green and shared neighbors in red.*

Table 2: *Fractional Distribution of QNA Pairs (%) Across HA Indices for Cu, Fe, Ni, and Ta*

Ha index	Cu (%)	Fe (%)	Ni (%)	Ta (%)
2441	72.26	72.87	72.52	71.47
2321	39.68	38.19	44.24	32.47
2431	99.31	99.57	99.45	99.58
2451	3.21	1.27	2.78	1.61
2331	0.17	0.04	0.15	0.04
2311	98.50	100.00	97.21	96.43
2211	0.02	0.01	0.07	0

To better understand the varying fractional distribution of QNA pairs across different HA Indices, we calculated the average thermal energy, defined here as the sum of the kinetic and potential energies, of central atoms for different HA Indices in Cu, Fe, Ni, and Ta MGs. This approach provided a representative and comprehensive assessment of the thermal energy associated with each HA index. These calculations are shown in *Fig. 11(a-d).* The results consistently indicate that the 2331 pair has the lowest energy across all systems, with Ta MG having the lowest energy. However, both the 2321 and 2311 pairs exhibit high thermal energy, indicating their instability. Nevertheless, their fraction in the system is negligible compared to the 2331 pair, suggesting that the 3-atom connection mode generally has low energy. This is consistent with prior studies [53, 54], and highlights the important role of the 2331 pair in stabilizing the MG structure. Furthermore, the 2451 and 2441 pairs have comparable energies, with 2451 being slightly lower.

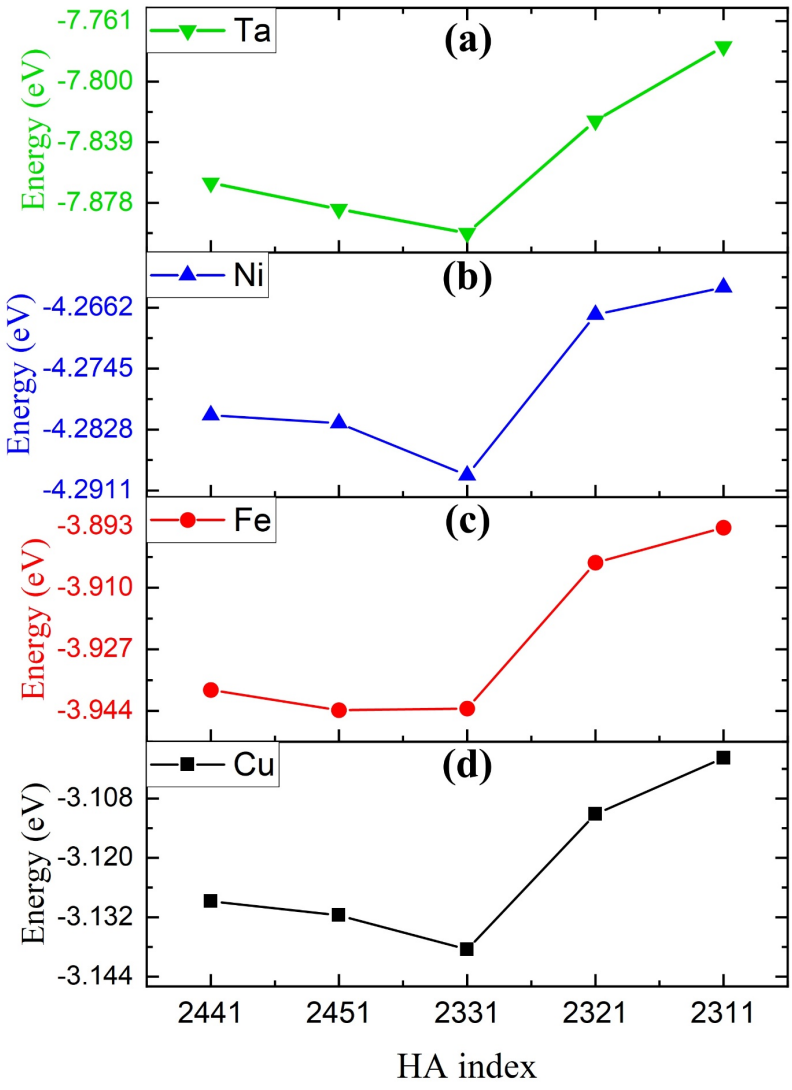

Fig. 11: Average thermal energy of central atoms plotted against HA index for monoatomic MGs of (a) Cu, (b) Fe, (c) Ni, and (d) Ta.

3-7. Mechanical behavior under tensile deformation

We performed uniaxial tensile simulations under periodic boundary conditions on all four monoatomic MGs and analyzed the deformed samples at 12% strain as a function of their initial N_Q values in the as-quenched samples. A mechanical hierarchy is evident in the stress-strain curves shown in *Fig. 12(a)*. At low strain, all four systems respond elastically before yielding and undergoing plastic deformation. After yielding the stress plateaus, with Ta showing the highest flow stress (~4.0 GPa at 0.06 strain, stabilizing around ~3.0 GPa in the plastic regime), followed by Fe and Ni with intermediate and moderately overlapping responses (~2.2-2.7 GPa), while Cu has the lowest strength (~1.3-1.5 GPa throughout deformation), consistent with its looser atomic packing. While Ta's denser initial packing ($\langle AN_Q \rangle$ = 0.694, *Table 1*) corresponds with its highest strength, this correlation is not strictly monotonic across all four systems, so factors beyond average packing density, such as the spatial distribution and connectivity of icosahedral clusters, must also influence the macroscopic mechanical response [75]. To understand local deformation mechanisms, we classified atoms by their initial N_Q values and tracked their local mechanical state during plastic deformation, and calculated the von Mises stress and hydrostatic stress for each atom i from its atomic stress tensor ($\sigma_{ij}(i)$) computed using the virial formulation [76]. The hydrostatic stress ($\sigma_{hyd}(i)$), which represents the volumetric (dilatational) component of the stress state, was calculated as:

$$\sigma_{hyd}(i) = \frac{\sigma_{xx}(i) + \sigma_{yy}(i) + \sigma_{zz}(i)}{3} \tag{7}$$

Where $\sigma_{xx}(i)$, $\sigma_{yy}(i)$, and $\sigma_{zz}(i)$ are the normal stress components for atom i along the x, y, and z directions. The deviatoric stress components $\left(s_x(i), s_y(i), s_z(i)\right)$ representing the shape-changing part of the stress, were then obtained by subtracting the hydrostatic stress: $s_j(i)$ = $\sigma_{jj}(i)$ - $\sigma_{hyd}(i)$. The von Mises stress ($\sigma_{vm}(i)$), which quantifies the equivalent stress driving plastic deformation, was calculated from the deviatoric components as [77, 78]:

$$\sigma_{vm}(i) = \sqrt{\frac{3}{2}\left(s_x(i)^2 + s_y(i)^2 + s_z(i)^2 + 2\left(\sigma_{xy}(i)^2 + \sigma_{xz}(i)^2 + \sigma_{yz}(i)^2\right)\right)} \tag{8}$$

where $\sigma_{xy}(i)$, $\sigma_{xz}(i)$, and $\sigma_{yz}(i)$ are the shear stress components for atom i.

The local von Mises stress, calculated from the atomic stress tensor components shown in *Fig. 12(c)*, ranges from 16-25 GPa, and shows that densely packed atoms ($N_Q = 0$) consistently carry the highest local stress: Ni (24.60 GPa), Ta (21.03 GPa), Fe (19.38 GPa), and Cu (16.60 GPa), decreasing by 0.8-1.8% as N_Q increases to 4, confirming that dense regions function as load-bearing frameworks that support higher stress concentrations. In contrast, shear strain exhibits the opposite trend, increasing monotonically with N_Q across all systems, with atoms at N_Q=0 experiencing the lowest shear strain (Ta: 0.143, Fe: 0.157, Ni: 0.180, Cu: 0.202) and rising by approximately 7-13% to N_Q = 4 (see *Fig. 12(b)*). While all atoms are undergoing plastic deformation at this strain level, the systematic variation demonstrates that loosely packed regions identified by QNA in the as-quenched glass accommodate significantly more plastic shear than densely packed regions, consistent with prior studies showing that introducing more loosely packed regions facilitates local shear transformations and inelastic events [79, 80], while tightly packed icosahedral clusters form rigid networks that resist shear rearrangements [80, 81]. The inverse correlation between von Mises stress and shear strain reveals the following plasticity mechanism: high-stress icosahedral (dense) regions resist plastic flow more effectively, accumulating stress while undergoing relatively less shear, thereby transferring load to neighboring high-N_Q regions that accommodate larger plastic strains at lower stress levels. This establishes a clear mechanical dichotomy where low N_Q atoms function as "stiff plastic carriers" that are load-bearing, icosahedrally ordered regions exhibiting high von Mises stress and undergoing relatively less shear, whereas high N_Q atoms form "compliant plastic zones" with lower stress and higher shear strain that serve as preferential sites for shear-transformation zones [79, 82]. Additionally, the hydrostatic stress exhibits distinct volumetric behaviors for the four systems. Both Ta and Fe MGs maintain a positive hydrostatic stress, which increases significantly as N_Q increases from 0 to 4, with the stress in Ta rising from 0.552 GPa to 1.009 GPa, and that in Fe from 0.281 GPa to 0.879 GPa. This indicates that loosely packed regions dilate under tension. The hydrostatic stress of Ni is negligible at N_Q = 0 (-0.017 GPa), and reaches 0.513 GPa at N_Q = 4, while that of Cu shows a modest overall variation, reaching 0.2 GPa at N_Q = 3 before decreasing to 0.066 GPa at N_Q = 4. The small magnitude of the Cu stress suggests a more homogeneous volumetric response, independent of local packing density. The significant increase in hydrostatic stress with N_Q in Ta and Fe MGs shows that systems with pronounced packing heterogeneity (high skewness in AN_Q distribution, *Table 1*) develop strong hydrostatic stress gradients during deformation, with loosely packed defects experiencing significant volumetric dilation. These results confirm the relevance of the QNA metric as a predictive structural indicator, establishing that the quantified structural defects in

the as-quenched glass determine both the stress distribution and the plastic activity during deformation. In particular, the superior strength of Ta derives from its high fraction (48%) of stable atoms with $N_Q = 0$, which form a rigid, percolating icosahedral network that more effectively resists plastic shear, while plastic flow concentrates in the high-N_Q regions for all monoatomic MGs.

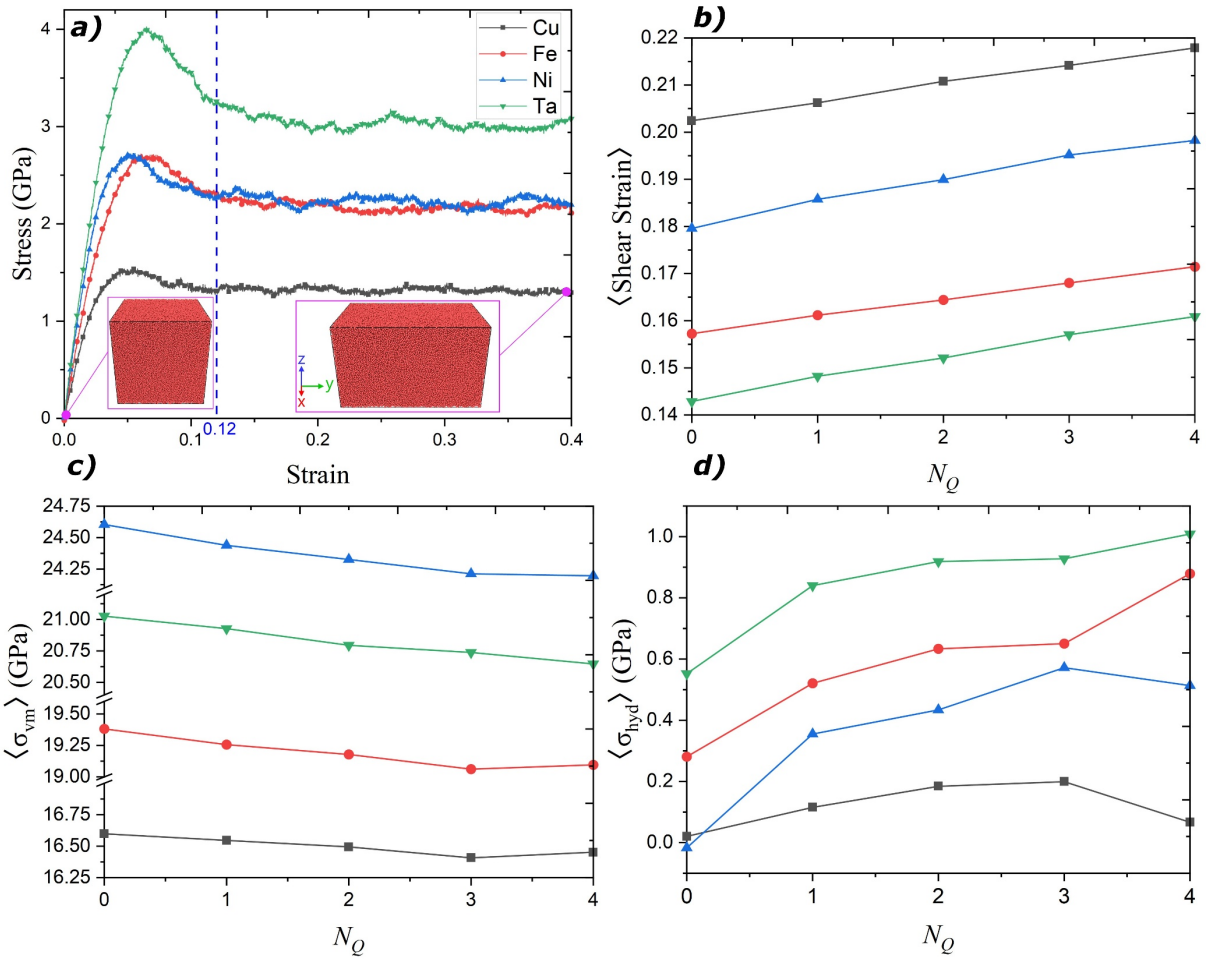

Fig. 12: *Mechanical response grouped by initial N_Q: (a) Stress–strain curves, with inset atomic snapshots of the Cu MG before deformation and at 0.40 strain; (b) Mean atomic shear strain versus N_Q at 12% strain; (c) Mean local von Mises stress versus N_Q; (d) Mean hydrostatic stress versus N_Q.*

4. Discussion

The structural analyses presented here highlight a clear link between local packing geometry and mechanical response. Loosely packed atoms, identified by QNA, simultaneously exhibit disrupted MRO in RDF (anomalous intermediate peak), unusual bond angles ($\theta \approx 90°$), reduced five-fold symmetry, and a preference for energetically unfavorable 2- and 4-atom connection modes compared to stable 2331 pairs. This explains why high-N_Q regions absorb more shear strain under tensile loading, as they lack the rigid icosahedral networks that resist plastic flow.

These high-N_Q regions, rich in defects, thus constitute preferential sites for the nucleation of shear transformation zones [83], in line with the established idea that these shear transformation zones initiate at free-volume sites in MGs [75, 79]. The load-bearing role we observe for low N_Q regions is consistent with the results of Wakeda and Shibutani [84], who showed that atoms within interpenetrating icosahedral clusters possess higher local elastic moduli than independent icosahedra or lower coordinate polyhedra. The icosahedral network has been described as forming a 'stiff backbone' that resists local shear deformation, explaining why N_Q = 0 atoms, which have the highest ⟨0,0,12,0⟩ fraction, carry the highest von Mises stress in a tensile test [80, 85].

The statistical descriptors in *Table 1* broadly correlate with mechanical performance, where Ta, which has the lowest AN_Q mean and variance, corresponds to the highest flow stress, while Cu, with the highest AN_Q mean, corresponds to the lowest strength. The dual skewness signature of Ta, characterized by a high Fisher-Pearson and low Pearson Median, reveals a structure dominated by stable N_Q = 0 atoms, with only a thin tail of defective regions. This explains both its exceptional strength and the pronounced hydrostatic stress gradients observed during deformation. The collapse of the normalized N_Q distributions onto a single curve for the four FCC and BCC systems studied (*Fig. 2(b)*), the similar *scf(r)* patterns across all four systems (*Fig. 5(a)*), as well as the constancy of the connection mode fractions that remain within ± 4% at each N_Q level (*Fig. 9(a-d)*), suggests that the packing topology in these monoatomic MGs is controlled by geometry rather than by element-specific bonding. The QNA parameter can therefore serve as a composition-independent structural descriptor for evaluating the mechanical behavior of MGs.

5. Conclusion

In summary, this work reveals how the QNA parameter captures the local and medium-range structural characteristics of monoatomic MGs. The four systems have different N_Q distributions, where Ta MG has nearly half of its atoms at N_Q = 0, indicating dense packing. In contrast, Cu MG contains more high N_Q atoms that cluster spatially into defect-rich pockets, serving as preferential sites for shear transformation zones during deformation. Voronoi analysis shows that the perfect icosahedral ⟨0,0,12,0⟩ polyhedron has the smallest average N_Q of all cluster types, while high N_Q atoms occupy distorted polyhedra with fewer five-fold faces. This geometric difference appears both in pair correlations, where high N_Q atoms blur the gap between first and second peaks of the RDF, and in bond angles, where a ~90° peak not associated with icosahedral angles emerges. From the Honeycutt–Andersen analysis, QNA

pairs are exclusively associated with 3- and 4-atom connection modes (2441, 2321, 2431 and 2311 pairs), while the energetically stable 2331 pairs contain virtually no QNA. These results show that the QNA parameter identifies structurally and energetically unfavorable atomic environments. Tensile simulations further support these structural observations by demonstrating that the N_Q distribution statistics are broadly correlated with mechanical response, with Ta's dense packing yielding the highest strength and Cu's loose packing the lowest. Overall, QNA is a useful parameter for characterizing defect-like packing in MGs and for identifying broad trends in their mechanical behavior.

Declaration of competing interest

The authors declare that they have no known competing financial interests or personal relationships that could have appeared to influence the work reported in this paper.

Data availability

Data will be made available on request.

Reference

[1] Klement W, Willens RH, Duwez P. Non-crystalline Structure in Solidified Gold–Silicon Alloys. *Nature* 1960; 187: 869–870.

[2] Ding J, Patinet S, Falk ML, et al. Soft spots and their structural signature in a metallic glass. *Proceedings of the National Academy of Sciences* 2014; 111: 14052–14056.

[3] Atila A, Kbirou M, Ouaskit S, et al. On the presence of nanoscale heterogeneity in Al70Ni15Co15 metallic glass under pressure. *Journal of Non-Crystalline Solids* 2020; 550: 120381.

[4] Liu S, Wang L, Ge J, et al. Deformation-enhanced hierarchical multiscale structure heterogeneity in a Pd-Si bulk metallic glass. *Acta Materialia* 2020; 200: 42–55.

[5] Miracle DB. A structural model for metallic glasses. *Nature Mater* 2004; 3: 697–702.

[6] Hufnagel TC, Schuh CA, Falk ML. Deformation of metallic glasses: Recent developments in theory, simulations, and experiments. *Acta Materialia* 2016; 109: 375–393.

[7] Cheng YQ, Ma E. Atomic-level structure and structure–property relationship in metallic glasses. *Progress in Materials Science* 2011; 56: 379–473.

[8] Wang WH. The elastic properties, elastic models and elastic perspectives of metallic glasses. *Progress in Materials Science* 2012; 57: 487–656.

[9] Atila A, Sukhomlinov SV, Honecker MJ, et al. Plasticity of metallic glasses dictated by their state at the fragile-to-strong transition temperature. *Acta Materialia* 2025; 286: 120753.

[10] Pauly S, Gorantla S, Wang G, et al. Transformation-mediated ductility in CuZr-based bulk metallic glasses. *Nature Mater* 2010; 9: 473–477.

[11] Han K, Qiang J, Wang Y, et al. Zr-Al-Co-Cu bulk metallic glasses for biomedical devices applications. *Journal of Alloys and Compounds* 2017; 729: 144–149.

[12] Guo H, Yan PF, Wang YB, et al. Tensile ductility and necking of metallic glass. *Nature Mater* 2007; 6: 735–739.

[13] Zhang Z, Zhang S, Wang Q, et al. Intrinsic tensile ductility in strain hardening multiprincipal element metallic glass. *Proceedings of the National Academy of Sciences* 2024; 121: e2400200121.

[14] Schuh CA, Hufnagel TC, Ramamurty U. Mechanical behavior of amorphous alloys. *Acta Materialia* 2007; 55: 4067–4109.

[15] Zhou Z-Y, Yang Q, Yu H-B. Toward atomic-scale understanding of structure-dynamics-properties relations for metallic glasses. *Progress in Materials Science* 2024; 145: 101311.

[16] Turnbull D. Kinetics of Solidification of Supercooled Liquid Mercury Droplets. *The Journal of Chemical Physics* 1952; 20: 411–424.

[17] Cheng YQ, Ma E, Sheng HW. Atomic Level Structure in Multicomponent Bulk Metallic Glass. *Phys Rev Lett* 2009; 102: 245501.

[18] Greer AL. Confusion by design. *Nature* 1993; 366: 303–304.

[19] Inoue A. Stabilization of metallic supercooled liquid and bulk amorphous alloys. *Acta Materialia* 2000; 48: 279–306.

[20] Zhong L, Wang J, Sheng H, et al. Formation of monatomic metallic glasses through ultrafast liquid quenching. *Nature* 2014; 512: 177–180.

[21] Tong X, Zhang Y-E, Shang B-S, et al. Breaking the vitrification limitation of monatomic metals. *Nat Mater* 2024; 23: 1193–1199.

[22] Khmich A, Sbiaai K, Hasnaoui A. Structural behavior of Tantalum monatomic metallic glass. *Journal of Non-Crystalline Solids* 2019; 510: 81–92.

[23] Peng HL, Li MZ, Wang WH. Structural Signature of Plastic Deformation in Metallic Glasses. *Phys Rev Lett* 2011; 106: 135503.

[24] Liu XJ, Xu Y, Hui X, et al. Metallic Liquids and Glasses: Atomic Order and Global Packing. *Phys Rev Lett* 2010; 105: 155501.

[25] Cohen MH, Grest GS. Liquid-glass transition, a free-volume approach. *Phys Rev B* 1979; 20: 1077–1098.

[26] Egami T. Atomic level stresses. *Progress in Materials Science* 2011; 56: 637–653.

[27] Kumar G, Neibecker P, Liu YH, et al. Critical fictive temperature for plasticity in metallic glasses. *Nat Commun* 2013; 4: 1536.

[28] Johnson WL, Demetriou MD, Harmon JS, et al. Rheology and Ultrasonic Properties of Metallic Glass-Forming Liquids: A Potential Energy Landscape Perspective. *MRS Bulletin* 2007; 32: 644–650.

[29] Ma E. Tuning order in disorder. *Nature Mater* 2015; 14: 547–552.

[30] Atila A, Wang Z, Riechers B, et al. Microstructure-specific mechanisms define multistage relaxation dynamics in a metallic model-glass. Epub ahead of print 29 May 2026. DOI: 10.48550/arXiv.2606.00323.

[31] Ding J, Cheng Y-Q, Sheng H, et al. Universal structural parameter to quantitatively predict metallic glass properties. *Nat Commun* 2016; 7: 13733.

[32] Nagel C, Rätzke K, Schmidtke E, et al. Free-volume changes in the bulk metallic glass Zr46.7Ti8.3Cu7.5Ni10Be27.5 and the undercooled liquid. *Physical Review B* 1998; 57: 10224–10227.

[33] Ye JC, Lu J, Liu CT, et al. Atomistic free-volume zones and inelastic deformation of metallic glasses. *Nature Mater* 2010; 9: 619–623.

[34] Wang Y, Li M, Xu J. Free volume gradient effect on mechanical properties of metallic glasses. *Scripta Materialia* 2017; 130: 12–16.

[35] Egami T. Understanding the properties and structure of metallic glasses at the atomic level. *JOM* 2010; 62: 70–75.

[36] Pan SP, Feng SD, Qiao JW, et al. Correlation between local structure and dynamic heterogeneity in a metallic glass-forming liquid. *Journal of Alloys and Compounds* 2016; 664: 65–70.

[37] Pan SP, Feng S-D, Wang L-M, et al. Structural disorder in metallic glass-forming liquids. *Sci Rep* 2016; 6: 27708.

[38] Pan S, Feng S, Qiao J, et al. Correlation between initial structure and athermal quasi-static compressive deformation in a metallic glass. *Journal of Alloys and Compounds* 2017; 699: 274–277.

[39] Pan S, Zheng G-P, Qiao J, et al. Bond-breaking analyses on the characteristics of flow defects in metallic glasses under plastic deformation. *Journal of Alloys and Compounds* 2019; 799: 450–461.

[40] Luo X, Zhang X, Pan S, et al. Multiple structural factors to influence the dynamics of icosahedral clusters in the Al90Sm10 super-cooled metallic liquid. *Journal of Non-Crystalline Solids* 2021; 565: 120848.

[41] Niu X, Yao G, Qiao J, et al. Effect of Y on the structure-property relationship of Mg65Cu25Y10 metallic glass. *Computational Materials Science* 2020; 171: 109285.

[42] Plimpton S. Fast Parallel Algorithms for Short-Range Molecular Dynamics. *Journal of Computational Physics* 1995; 117: 1–19.

[43] Mendelev MI, Kramer MJ, Becker CA, et al. Analysis of Semi-Empirical Interatomic Potentials Appropriate for Simulation of Crystalline and Liquid Al and Cu. *Philosophical Magazine* 2008; 88: 1723–1750.

[44] Mishin Y. Atomistic modeling of the γ and γ′-phases of the Ni–Al system. *Acta Materialia* 2004; 52: 1451–1467.

[45] Mendelev MI, Han S, Srolovitz DJ, et al. Development of new interatomic potentials appropriate for crystalline and liquid iron. *Philosophical Magazine* 2003; 83: 3977–3994.

[46] Ravelo R, Germann TC, Guerrero O, et al. Shock-induced plasticity in tantalum single crystals: Interatomic potentials and large-scale molecular-dynamics simulations. *Phys Rev B* 2013; 88: 134101.

[47] Atila A, Bitzek E. Atomistic origins of deformation-induced structural anisotropy in metaphosphate glasses and its influence on mechanical properties. *Journal of Non-Crystalline Solids* 2024; 627: 122822.

[48] Ganisetti S, Atila A, Guénolé J, et al. The origin of deformation induced topological anisotropy in silica glass. *Acta Materialia* 2023; 257: 119108.

[49] Pan Z, Atila A, Bitzek E, et al. Topology of anisotropic glasses from persistent homology analysis. *Journal of Non-Crystalline Solids* 2024; 627: 122801.

[50] Stukowski A. Visualization and analysis of atomistic simulation data with OVITO–the Open Visualization Tool. *Modelling and Simulation in Materials Science and Engineering* 2009; 18: 015012.

[51] Niu X, Feng S, Pan S. Related Structure Characters and Stability of Structural Defects in a Metallic Glass. *Materials (Basel)* 2018; 11: 468.

[52] Ding J, Ma E, Asta M, et al. Second-Nearest-Neighbor Correlations from Connection of Atomic Packing Motifs in Metallic Glasses and Liquids. *Sci Rep* 2015; 5: 17429.

[53] Houba A, El Ayoubi M, Samiri A, et al. Short and medium range order in the rapidly solidified metallic liquid Ta: Atomic packing, connection modes, and pressure effect. *Materialia* 2024; 38: 102270.

[54] El Ayoubi M, Khmich A, Samiri A, et al. Investigating medium range order in Mg-Al binary metallic glasses: Molecular dynamics approach. *Journal of Non-Crystalline Solids* 2023; 621: 122620.

[55] Hafner J. BOND-ANGLE DISTRIBUTION FUNCTIONS IN METALLIC GLASSES. *J Phys Colloques* 1985; 46: C9-78.

[56] Haouas H, Khmich A, Samiri A, et al. On the structural changes and glass transition temperature relationship during the formation of Re-W metallic glasses. *Journal of Non-Crystalline Solids* 2021; 557: 120571.

[57] Ganesh P, Widom M. Signature of nearly icosahedral structures in liquid and supercooled liquid copper. *Phys Rev B* 2006; 74: 134205.

[58] Chen Y. Spatial autocorrelation equation based on Moran's index. *Sci Rep* 2023; 13: 19296.

[59] Chen Y. New Approaches for Calculating Moran's Index of Spatial Autocorrelation. *PLOS ONE* 2013; 8: e68336.

[60] Mo J, Liu H, Zhang Y, et al. Effects of pressure on structure and mechanical property in monatomic metallic glass. *Journal of Non-Crystalline Solids* 2017; 464: 1–4.

[61] Qin X, Wu JQ, Li MZ. Atomic structural characteristics and dynamical properties in monatomic metallic liquids via molecular dynamics simulations. Epub ahead of print 5 April 2022. DOI: 10.48550/arXiv.2204.01944.

[62] Li F, Zhang J, Xu X, et al. Influence from connection of atomic clusters on the second peak splitting of pair distribution function in metallic glasses. *Journal of Non-Crystalline Solids* 2023; 600: 122021.

[63] Kbirou M, Atila A, Hasnaoui A. On the structure and icosahedral interconnectivity in Tantalum monatomic glass produced under pressure. *Phys Scr* 2024; 99: 085946.

[64] Dmowski W, Iwashita T, Chuang C-P, et al. Elastic Heterogeneity in Metallic Glasses. *Phys Rev Lett* 2010; 105: 205502.

[65] Zhang YE, Tong X, Zhang HP, et al. Evidence of intrinsic structural heterogeneity by monatomic metallic glass. *Scripta Materialia* 2024; 252: 116261.

[66] Chen Y, Jiang M, Dai L. How does the initial free volume distribution affect shear band formation in metallic glass? *Sci China Phys Mech Astron* 2011; 54: 1488–1494.

[67] Wang JG, Zhao DQ, Pan MX, et al. Correlation between onset of yielding and free volume in metallic glasses. *Scripta Materialia* 2010; 62: 477–480.

[68] Dong Y, Fecht H-J. Deformation of Nanoglass under High-pressure Torsion. *J Nanotechnol Nanomaterials* 2022; Volume 3: 1–7.

[69] Wu SQ, Wang CZ, Hao SG, et al. Energetics of local clusters in Cu64.5Zr35.5 metallic liquid and glass. *Applied Physics Letters* 2010; 97: 021901.

[70] Guo G. Quasi-Icosahedral Clusters in Zr-Based Metallic Glasses. *Metals* 2020; 10: 1135.

[71] Amigo N. Temperature and composition effects on the structure and mechanical behavior of V-Al metallic glasses. *Journal of Molecular Modeling* 2025; 32: 1.

[72] Li MZ, Peng HL, Hu YC, et al. Five-fold local symmetry in metallic liquids and glasses. *Chinese Phys B* 2017; 26: 016104.

[73] Honeycutt JD, Andersen HC. Molecular dynamics study of melting and freezing of small Lennard-Jones clusters. *J Phys Chem* 1987; 91: 4950–4963.

[74] Zhang L, Wu Y, Feng S, et al. Rejuvenated metallic glass strips produced *via* twin-roll casting. *Journal of Materials Science & Technology* 2020; 38: 73–79.

[75] Gu Y, Cappola J, Wang J, et al. A Hall-Petch-like relationship linking nanoscale heterogeneity to yield stress of heterogeneous metallic glasses. *International Journal of Plasticity* 2023; 170: 103759.

[76] Thompson AP, Plimpton SJ, Mattson W. General formulation of pressure and stress tensor for arbitrary many-body interaction potentials under periodic boundary conditions. *J Chem Phys* 2009; 131: 154107.

[77] Hu YC, Guan PF, Li MZ, et al. Unveiling atomic-scale features of inherent heterogeneity in metallic glass by molecular dynamics simulations. *Phys Rev B* 2016; 93: 214202.

[78] Zhou G, Huang Q, Chen Y, et al. Annihilation Mechanism of Low-Angle Grain Boundary in Nanocrystalline Metals. *Metals* 2022; 12: 451.

[79] Pan D, Inoue A, Sakurai T, et al. Experimental characterization of shear transformation zones for plastic flow of bulk metallic glasses. *Proceedings of the National Academy of Sciences* 2008; 105: 14769–14772.

[80] Lee M, Lee C-M, Lee K-R, et al. Networked interpenetrating connections of icosahedra: Effects on shear transformations in metallic glass. *Acta Materialia* 2011; 59: 159–170.

[81] Zhou Y-N, Yang Z-Y, Dai L-H. Uncovering the structural origin of shear banding in metallic glasses via tracing back to the critical glass transition process. *Phys Rev Mater* 2024; 8: 073603.

[82] Wu Y, Cao D, Yao Y, et al. Substantially enhanced plasticity of bulk metallic glasses by densifying local atomic packing. *Nat Commun* 2021; 12: 6582.

[83] Long T, Long Z, Pang B. Uncovering the microstructural origins of shear transformation events in metallic glasses: Insights from combining knowledge and data. *Journal of Non-Crystalline Solids* 2025; 653: 123419.

[84] Wakeda M, Shibutani Y. Icosahedral clustering with medium-range order and local elastic properties of amorphous metals. *Acta Materialia* 2010; 58: 3963–3969.

[85] Ding J, Cheng Y-Q, Ma E. Full icosahedra dominate local order in Cu64Zr34 metallic glass and supercooled liquid. *Acta Materialia* 2014; 69: 343–354.